Inorganic Chemistry

ARTICLE

pubs.acs.org/IC

Influence of Crystallization State and Microstructure on the Chemical Durability of Cerium−Neodymium Mixed Oxides

Laurent Claparede,[†,‡] Nicolas Clavier,[†] Nicolas Dacheux,[*,†] Philippe Moisy,[‡] Renaud Podor,[†] and Johann Ravaux[†]

[†]ICSM, UMR5257 CNRS/CEA/UM2/ENSCM, Site de Marcoule, Bât. 426, BP 17171, 30207 Bagnols/Cèze, France

[‡]CEA, Nuclear Energy Division, RadioChemistry & Processes Department, BP 17171, 30207 Bagnols/Cèze, France

ABSTRACT: To underline the potential links between the crystallization state and the microstructure of powdered cerium−neodymium oxides and their chemical durability, several $Ce^{IV}_{1-x}Nd^{III}_{x}O_{2-x/2}$ mixed dioxides were prepared in various operating conditions from oxalate precursors and then leached. The powdered samples were first examined through several physicochemical properties (crystallization state and associated crystallite size, reactive surface area, porosity...). The dependence of the normalized dissolution rates on various parameters (including temperature, nitric acid concentration, crystallization state) was examined for pure CeO_2 and $Ce_{1-x}Nd_xO_{2-x/2}$ solid solutions (with $x = 0.09$ and 0.16). For CeO_2, either the partial order related to the proton activity ($n = 0.63$) or the activation energy ($E_A = 37$ kJ·mol^{-1}) suggested that the dissolution was mainly driven by surface reactions occurring at the solid−liquid interface. The chemical durability of the cerium−neodymium oxides was also strongly affected by chemical composition. The initial normalized dissolution rates were also found to slightly depend on the crystallization state of the powders, suggesting the role played by the crystal defects in the dissolution mechanisms. On the contrary, the crystallite size had no important effect on the chemical durability. Finally, the normalized dissolution rates measured near the establishment of saturation conditions were less affected, which may be due to the formation of a gelatinous protective layer at the solid/liquid interface.

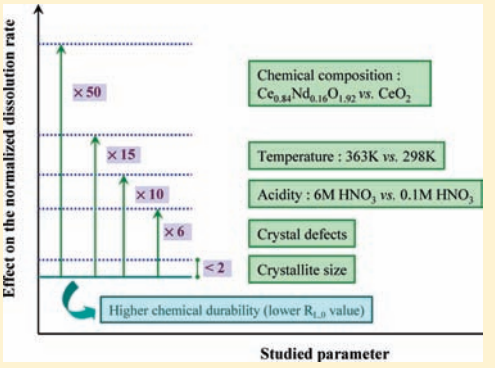

1. INTRODUCTION

Mixed actinide dioxides, such as $(U,Pu)O_2$, are already used as fuels in pressurized water reactors (PWRs) (including Gen III, EPR) and stand as potential fuels for several Gen IV concepts, such as sodium-cooled fast reactor (SFR) or gas-cooled fast reactor (GFR).[1,2] Moreover, as the reprocessing of actinides coming from nuclear spent fuel into new fuel elements has emerged to economize uranium resources, to reduce the long-term nuclear waste radiotoxicity, and to increase the resistance to plutonium proliferation, the recycling of minor actinides, including neptunium, americium, and curium, in such mixed-oxide fuels or in UO_2-based blankets surrounding the core is now often considered.[3]

Mixed actinide dioxide fuels are currently prepared through dry chemistry routes based on powder mixtures, which could result in some heterogeneity in the cationic distribution in the material.[4] More recently, various studies were dedicated to the preparation of homogeneous solids through wet chemistry methods based on the precipitation of crystallized precursors.[5] Among them, carbonates,[6] nitrates,[7] or hydroxides[8] were reported in the literature. However, oxalate compounds remain probably the most frequently cited due to their quantitative precipitation and to the good properties they confer to the final solids obtained after heating (i.e., cationic distribution in the structure, sintering capability, or chemical durability).[9,10] Indeed, such physicochemical properties of the mixed dioxides need to be optimized in order to fit with the severe environments planned in the Gen IV-type reactor concepts.[11]

In this context, it appeared important to evaluate the consequences of the modifications linked to the initial precipitation of oxalate precursors on several properties of interest and, particularly, on dissolution kinetics, which stands as a key parameter for the reprocessing operations. Consequently, this general study was undertaken to highlight the links between the structure and the microstructure of $Ce_{1-x}Nd_xO_{2-x/2}$ model dioxide materials and their ability to dissolve. Indeed, CeO_2 is frequently used as a surrogate for plutonium dioxide[12] since both oxides crystallize in the same fluorite-type structure (face-centered cubic; space group, $Fm\bar{3}m$; JCPDS cards 01-081-0792 for CeO_2 and 00-051-0798 for PuO_2) with close unit cell parameters (Table 1) due to similar ionic radii ($^{VIII}r_{Ce^{4+}} = 0.97$ Å and $^{VIII}r_{Pu^{4+}} = 0.96$ Å[13]). Similarly, neodymium ($^{VIII}r_{Nd^{3+}} = 1.109$ Å) can be used to mimic the behavior of trivalent minor actinides, such as americium ($^{VIII}r_{Am^{3+}} = 1.09$ Å) and curium.[14−17]

Some studies already showed that several parameters, such as density, porosity, grain size, or density of grain boundaries, could have a significant impact on the normalized dissolution rates.[9,23]

Received: June 13, 2011
Published: August 02, 2011

Table 1. Unit Cell Parameter (a) of Dioxides Crystallized in the Fluorite-Type Structure

	CeO_2	ThO_2	UO_2	NpO_2	PuO_2	AmO_2
^{VIII}r(cat) (Å)[13]	0.97	1.05	1.00	0.98	0.96	0.95
a (Å)	5.4104(2)	5.597(2)	5.469(1)	5.433(1)	5.395(1)	5.3736(5)
reference	18	19	20	21	21	22

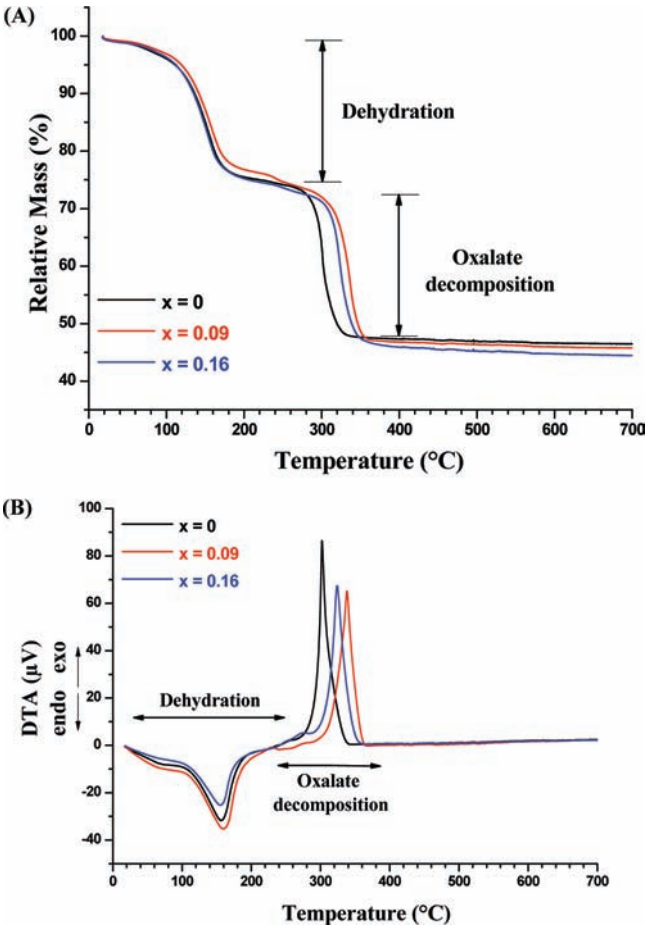

Figure 1. Results of TGA (a) and DTA (b) obtained when heating $Ce_{2-2x}Nd_{2x}(C_2O_4)_3 \cdot 10H_2O$ ($x = 0$, 0.09, and 0.16) in air with a heating rate of 5 °C min^{-1}.

However, they were poorly examined compared to the well-known effects of temperature or pH in the literature. Indeed, many studies were dedicated to the optimization of the operating conditions for the dissolution of PuO_2[24−26] even if the conclusions on the mechanisms involved were far less numerous. Nevertheless, they all demonstrated the refractory nature of plutonium dioxide in both oxidative and reducing conditions.[27,28] In comparison, the dissolution of CeO_2 was relatively poorly examined. Cerium dioxide was generally reported to be strongly resistant to corrosion in nitric acid media. However, the formation of nitrate complexes promoting the ceria dissolution was already mentioned. Indeed, few studies reported the experimental conditions leading to the quantitative dissolution of cerium dioxide and established the associated kinetics.[29,30] Moreover, the reaction of the dissolution of CeO_2 in noncomplexing acid solutions is not thermodynamically favorable. The calculation of the free enthalpy variation of the dissolution reaction without any change in the oxidation state (eq 1) led to a positive variation of the Gibbs energy:[31]

$$CeO_2 + 4H^+ \leftrightarrow Ce^{4+} + 2H_2O$$
$$\Delta_R G^\circ = 40.1\ kJ \cdot mol^{-1} \quad (1)$$

After the preparation of a panel of powdered CeO_2 and $Ce_{1-x}Nd_xO_{2-x/2}$ samples, this work was thus mainly dedicated to the influence of their crystallization state on their normalized dissolution rate in acid solutions. Its relative promoting role was compared to that of temperature or acid concentration.

2. EXPERIMENTAL SECTION

2.1. Synthesis of Cerium(IV)−Neodymium(III) Oxide Solid Solutions. Chemical reagents were supplied by VWR, and Aldrich-Fluka, whereas cerium(III) or neodymium(III) chloride hexahydrates were issued from Strem Chemicals (≥99.9% purity). These latter were dissolved in 0.5 M HNO_3 to obtain solutions with a final concentration of 0.1 M in cations. The synthesis of the initial oxalate precursors was performed through a mixture of Ce (III) and Nd (III) solutions in the desired stoichiometry (mole ratios of $x = 0$, 0.1, and 0.2) with a large excess of oxalic acid at room temperature, under stirring. The quantitative precipitation of the cations occurred immediately according to the following chemical reaction:

$$(2-2x)Ce^{3+} + 2xNd^{3+} + 3H_2C_2O_4 + yH_2O \rightarrow Ce_{2-2x}Nd_{2x}(C_2O_4)_3 \cdot yH_2O + 6H^+ \quad (2)$$

Mixed oxalate precipitates were then washed several times with deionized water, filtered, and dried overnight in an oven (90 °C). Whatever the chemical composition considered, XRD patterns revealed that the samples prepared were single phase and fitted well with all the XRD lines associated with the lanthanide oxalate decahydrate $Ln_2(C_2O_4)_3 \cdot 10\ H_2O$ (Ln = La−Er; monoclinic structure; space group, $P2_1/c$).[32,33]

The transformation of (Ce,Nd)-oxalate into a mixed dioxide was then followed through thermogravimetric analysis (TGA) and differential thermal analysis (DTA) (Figure 1), performed on a Setsys Evolution apparatus provided by Setaram. Heating treatments were performed in air, with a constant rate of 5 °C $\cdot min^{-1}$ up to 300−1200 °C, identical to that applied for the preparation of final oxides.

2.2. Characterization. To evaluate the influence of the crystallization state on several physicochemical properties of powdered $Ce_{1-x}Nd_xO_{2-x/2}$ samples, oxalate precursors were fired for 2 h at different temperatures ranging from 300 to 1200 °C, and the resulting samples were extensively characterized.

X-ray Powder Diffraction. XRD patterns were collected between 10 and 80° ($\theta-2\theta$ mode) using a Bruker D8 Advance X-ray diffractometer (Cu $K\alpha_{1,2}$ radiation, λ = 1.5418 Å) equipped with a linear Lynx-eye detector. For all the powdered samples, a step of 0.01° and a counting time of 1.5 s $\cdot step^{-1}$ were considered. The unit cell parameters for fluorite-type $Ce_{1-x}Nd_xO_{2-x/2}$ oxides were refined by the Rietveld method using the Thomson−Cox−Hastings Pseudo Voigt convoluted with an axial divergence asymmetry function[34] available in the Fullprof_Suite program.[35]

ESEM. In situ high-temperature environmental scanning electron microscopy (HT-ESEM) experiments were performed using a field emission gun environmental scanning electron microscope (model FEI QUANTA 200 ESEM FEG) equipped with a 1500 °C hot stage. The sample was directly placed in a 5 mm diameter MgO crucible covered

dx.doi.org/10.1021/ic201269c |Inorg. Chem. 2011, 50, 9059–9072

Table 2. Expected and Experimental Compositions of Fluorine-Type $Ce_{1-x}Nd_xO_{2-x/2}$ and Associated Refined Unit Cell Parameters

expected chemical formula ($Ce_{1-x}Nd_xO_{2-x/2}$)	x (exptl) (from EDS)	unit cell parameter (Å)
$x = 0$	0	$a = 5.4107(2)$
$x = 0.1$	0.09	$a = 5.4305(4)$
$x = 0.2$	0.16	$a = 5.4489(1)$

with platinum paint. The sample was heated directly in the ESEM chamber with a rate of 20 °C·min^{-1} and considering several holding temperatures between room temperature and 1000 °C. The furnace temperature was controlled by a thermocouple placed near the MgO crucible, and the sample temperature accuracy was checked during each experiment. Micrographs were recorded each 100 °C all during the heat treatment of the sample on a selected part of the ceramic with different magnifications. The observations were performed in air atmosphere at an operating pressure of 120 Pa, and a specific detector was used for in situ gaseous secondary electron imaging at high temperature.

The precise chemical composition of the samples was checked by the means of energy dispersive spectrometry (EDS) coupled with the ESEM device. For this purpose, each compound was previously shaped through uniaxial pressure, sintered for 10 h at 1400 °C in air, then coated with an epoxy resin, polished, and finally metalized by carbon deposition. EDS analyses were then performed considering 12 data acquisitions. At least 40 000 counts spectra were collected by the EDS detector using an optimal working distance of 11.4 mm and an acceleration voltage of 15 kV. In these conditions, the average x_{Nd} value was assumed with an absolute accuracy of ±0.01 since all the data acquisitions only led to a weak dispersion.

The results of characterization of $Ce_{1-x}Nd_xO_{2-x/2}$ samples by X-EDS are gathered in Table 2. From these results, all the samples were found to be homogeneous and single phase. Only slight deviations in the chemical compositions of $Ce_{1-x}Nd_xO_{2-x/2}$ were noted compared to the calculated values.

Specific Surface Area and Porosity Distribution. The specific surface area measurements were performed with a Micromeritics ASAP 2020 apparatus using nitrogen adsorption (Brunauer, Emmet, and Teller, BET method) at 77 K. The pore size distribution of the oxide samples were estimated from the desorption branches of the nitrogen sorption isotherm according to the BJH (Barret, Joyner, and Halenda) method, based on the Kelvin equation, which correlates the pore size with critical condensation pressure, and by assuming a straight cylindrical pore model (that is not always the case for all the studied materials).[36] Prior to the measurements, the samples were dried at 300 °C for 3 h to ensure their complete outgassing.

2.3. Leaching Experiments. Leaching tests were performed using batch experiments in polytetrafluoroethylene containers at room temperature. For each dissolution experiment, about 125 mg of powder was put in contact with 25 mL of 0.1−6 M HNO_3 for a few weeks to several months. After settling, an aliquot of 700 μL of the leachate was taken off, then renewed with fresh solution at regular intervals to determine the evolution of the elementary releases. In such conditions, less than 3% of the leachate was removed in order to avoid any perturbation in the establishment of saturation processes at the solid/liquid interface. Aliquots were then centrifuged at 12 000 rpm to avoid the presence of colloids smaller than 11 nm.[37]

Furthermore, the behavior of $Ce_{1-x}Nd_xO_{2-x/2}$ samples during dissolution processes was also examined through leaching tests performed with high leachate renewals (1 mL·h^{-1}), called "dynamic" experiments (2 M HNO_3, T = 90 °C), in order to avoid any saturation processes. Finally, the concentrations of cerium and neodymium released in the leachate were determined by inductively-coupled plasma atomic emission spectroscopy (ICP-AES, Spectro Arcos) after dilution of the samples with diluted nitric acid in order to reach a total volume of analyzed solution of 6 mL. The intensity of the peaks was recorded at λ = 448.691 and 413.765 nm for cerium and at λ = 406.109 and 430.358 nm for neodymium to avoid any interference between the elements.

The normalized weight losses (N_L, also called normalized leachings) were calculated from the elementary concentrations after normalization by the reactive surface S (m^2) of the sample in contact with the solution and by the weight stoichiometric ratio of the element considered in the solid (f_i, expressed as the ratio between the mass of the considered element and the overall mass of the sample),[38] following the equation

$$N_L(i) = \frac{m_i}{f_i \times S} \quad (3)$$

where m_i (expressed in g) corresponds to the total amount of the element i measured in the solution.

Using the approach described by Lasaga[39] and derivating eq 3 as a function of leaching time, the normalized dissolution rate of the element i was determined from[38]

$$R_L(i) = \frac{dN_L(i)}{dt} = \frac{1}{f_i \times S} \times \frac{dm_i}{dt} \quad (4)$$

In such conditions, the normalized dissolution rates correspond to the slopes obtained when plotting the evolution of the normalized weight losses. The normalized leachings N_L (expressed in g·m^{-2}) and the associated normalized dissolution rates R_L (expressed in g·m^{-2}·d^{-1}) were determined considering the following equation

$$R_L(i) = \frac{dN_L(i)}{dt} = \frac{d}{dt}\left(\frac{C_i \times V \times M_i}{f_i \times S}\right) \approx \frac{V \times M_i}{f_i \times S} \times \frac{dC_i}{dt} \quad (5)$$

where C_i is the concentration of the lanthanide in the leachate (mol·L^{-1}), V the volume of leachate (L), f_i the weight stoichiometric ratio of the lanthanide considered in the solid (dimensionless) and M_i its molar mass (g·mol^{-1}), and S the reactive surface of the solid (m^2).

In this expression, the stoichiometric ratio was assumed to remain almost constant during the leaching tests, which could not be systematically the case for all the ceramic materials. However, this assumption was supported by the strong refractory character of CeO_2,[29,30] and by the associated very low normalized dissolution rates determined, as reported in the following sections. On the basis of an average normalized dissolution rate of 10^{-5} g·m^{-2}·d^{-1}, less than 1% of the initial material would be dissolved after 100 days of leaching.

The normalized mass loss would increase linearly with time during the first days of leaching tests. However, the real behavior was often found rather different since an initial pulse in the elementary releases was observed. This phenomenon, which remained limited for these studied materials, was usually assigned to the presence of crystal defects, nonstoichiometric phases, minor phases, or small particles at the surface of the unwashed samples.[38,40,41] It usually produced large amounts of colloids during the first days of leaching tests. To avoid this problem, an initial washing of the samples was performed for 3 days in 2 M HNO_3 at room temperature, before the beginning of the dissolution experiments. Moreover, for longer leaching times (i.e., near the saturation conditions in the leachate), the precipitation of neoformed phases usually induced the formation of a protective layer acting as a diffusion barrier for the released elements, leading to the significant decrease of the associated normalized dissolution rates.

Thereafter, the reaction of dissolution is called stoichiometric if all the elements i are released in the leachate with the same normalized dissolution rate. Conversely, if one element is released more rapidly from the solid (e.g., like fluorine in the britholite structure[40]), the dissolution is called selective regarding to the considered element. Moreover, the dissolution is qualified as congruent when all the

dx.doi.org/10.1021/ic201269c |*Inorg. Chem.* 2011, 50, 9059–9072

Table 3. Partial Order Related to the Proton Activity and Activation Energy Obtained during the Dissolution of Several Ceramics, Minerals, and Materials

mineral/material	partial order n	reference	E_A (kJ·mol^{-1})	reference
albite ($NaAlSi_3O_8$)	0.49	50	71	56
β-TPD ($Th_4(PO_4)_4P_2O_7$)	0.31−0.35	53	42 ± 3	38
ThO_2	0.26 ± 0.05	48		
	0.41 ± 0.05	47	20 ± 3	47
UO_2	0.91 ± 0.09	48		
	0.53	57	35 ± 3	58
$Th_{0.63}U_{0.37}O_2$	0.30 ± 0.01	48		
	0.55 ± 0.10	47	33 ± 4	47
$Th_{0.87}Pu_{0.13}O_2$	0.50 ± 0.06	59	ND[a]	
$U_{0.75}Pu_{0.25}O_2$	1.7	27	10−32	27

[a] ND: not determined.

normalized dissolution rates are identical (i.e., when all the elements are released with the same ratios than the stoichiometry of the initial material). Conversely, it is called incongruent if at least one element is precipitated as neoformed phases in the back end of the initial reaction of dissolution. More generally, the dissolution is described as congruent for $1/3 < R_i/R_j < 3$.[41,42]

Influence of Acidity. Many authors already demonstrated that the normalized dissolution rates of most of the minerals increased with the proton concentration for pH < 7.[41−48] Indeed, in acid solutions, the R_L values were found to be proportional to a fractional power of the proton activity as follows[49−53]

$$R_L = k'_T \times (H_3O^+)^n = k'_T \times (\gamma_{H_3O^+} \times [H_3O^+])^n \quad (6)$$

where R_L refers to the proton-promoted normalized dissolution rate and k'_T (expressed in g·m^{-2}·day^{-1}) represents the apparent normalized dissolution rate constant at $-\log([H_3O^+]) = 0$. k'_T is independent of the acidity of the leachate, but temperature-dependent. The n parameter corresponds to the partial order related to the proton activity, (H_3O^+) to the proton activity, and γH_3O^+ corresponds to the proton activity coefficient. In this study, γH_3O^+ values were calculated according to the Pitzer and SIT models.[54] The values of partial orders related to protons, n (and to hydroxide ions in basic media), were generally found between 0 and 1 for several materials and minerals (Table 3), suggesting that the dissolution was mainly driven by surface reactions occurring at the solid−liquid interface.

Influence of Temperature. Temperature is also an important parameter affecting the normalized dissolution rate according to the Arrhenius law, that is

$$R_L = k \times e^{-(E_A/RT)} = k'' \times (H_3O^+)^n \times e^{-(E_A/RT)} \quad (7)$$

where k is the normalized dissolution rate constant independent of temperature (expressed in g·m^{-2}·day^{-1}) and E_A is the apparent activation energy of the dissolution of the mineral (expressed in kJ mol^{-1}). Plotting the variation of $\ln(R_L)$ versus the reciprocal temperature allows determining the activation energy and associated k value. Because of the formation of adsorbed species onto the leached surface, such E_A values were usually found to be significantly lower than the energy of formation of chemical bonds (Table 3).

Most of the available theories indicate that the reaction of dissolution is controlled by the decomposition of an activated complex[55] according to a three-step process:

(1) Adsorption of aqueous species onto the surface.
(2) Reaction of adsorbed species among themselves or with atoms of the surface.
(3) Desorption of the product species formed at the surface.

The last reaction is usually slower and, therefore, controls the overall rate of dissolution of the solid.

3. RESULTS AND DISCUSSION

3.1. Preparation of $Ce_{1-x}Nd_xO_{2-x/2}$ Solid Solutions. The final oxides were obtained after heating the lanthanide oxalate decahydrates $Ln_2(C_2O_4)_3 \cdot 10H_2O$ in air in alumina boats, according to the following chemical reaction:

$$Ce^{III}_{2-2x}Nd^{III}_{2x}(C_2O_4)_3 \cdot yH_2O \xrightarrow{\Delta} 2Ce^{IV}_{1-x}Nd^{III}_xO_{2-x/2} + (4-x)CO\uparrow + (2+x)CO_2\uparrow + yH_2O\uparrow \quad (8)$$

This chemical transformation was characterized by a strong change in the powder color from white to yellow, due to the oxidation of cerium(III) into cerium(IV). The chemical transformation of $Ce_{2-2x}Nd_{2x}(C_2O_4)_3 \cdot 10H_2O$ into $Ce_{1-x}Nd_xO_{2-x/2}$ was then followed through TGA/DTA experiments (Figure 1).

Whatever the chemical composition examined, the variation of the weight loss versus heating temperature exhibited two steps corresponding to a total loss of 53%, close to that calculated (52.5%). The first one (weight loss of 25%) occurred between 20 and 200 °C and was correlated to the loss of 10 water molecules, leading to the formation of anhydrous $Ce_{2-2x}Nd_{2x}(C_2O_4)_3$. The decomposition of oxalates occurred between 280 and 360 °C with the additional loss of CO and CO_2 molecules (experimental mass loss of 26%; calcd: 27%). This result was in good agreement with the observations made by several authors on the decomposition of cerium oxalate.[60,61] Conversely to what was observed during the thermal decomposition of mixed Ce and Gd oxalates,[60,61] the formation of carbonated or oxo-carbonated intermediates was not clearly evidenced in this study. Indeed, the data reported in Figure 1B indicate that the $Ce_{2-2x}Nd_{2x}(C_2O_4)_3 \cdot 10H_2O$ precipitates were fully converted to $Ce_{1-x}Nd_xO_{2-x/2}$ solid solutions when heating above 400 °C. Moreover, no endothermic peak associated with the formation of carbonate or oxocarbonate was observed prior to the formation of oxide. This result was also checked by in situ μ-Raman spectroscopy experiments on several lanthanide oxalates.

Moreover, the exothermic peak observed in the DTA curves and associated with the decomposition of oxalate entities (thus, to the release of CO and CO_2) was measured at higher temperature for $Ce_{2-2x}Nd_{2x}(C_2O_4)_3 \cdot 10H_2O$ samples than for $Ce_2(C_2O_4)_3 \cdot 10H_2O$. This result was consistent with the data reported all along the $Ce_{2-2x}Nd_{2x}(C_2O_4)_3 \cdot 10H_2O$ series,[62] where the temperature slightly increased when increasing the neodymium content (T = 310, 370, and 410 °C for x = 0, 0.285, and 0.59, respectively). It also agreed well with the data reported by Higashi et al.[61] and Sharov et al.,[63] who showed an increase of the decomposition temperature with the ionic radius of the rare-earth element during the decomposition of $Ce_{2-2x}Ln_{2x}(C_2O_4)_3 \cdot 10H_2O$ (Ln = Yb, Gd, Sm, Nd, La). The small difference observed between both solid solutions (ΔT = 15 °C) could result from the uncertainties associated with the temperature determination but could also arise from the small differences observed in the initial powder reactivity (S_{BET} = 2 and 5 m^2·g^{-1} for x = 0.09 and x = 0.16, respectively).

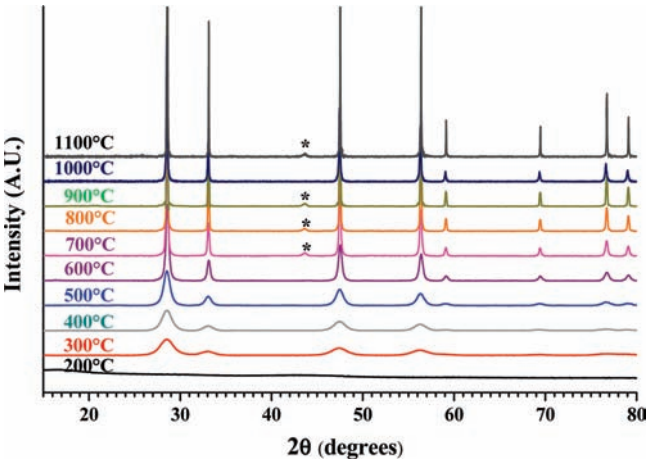

Figure 2. XRD patterns of CeO_2 recorded after heating the samples at various temperatures (air, 2 h). All the XRD lines of the sample holder are pointed out by stars (∗).

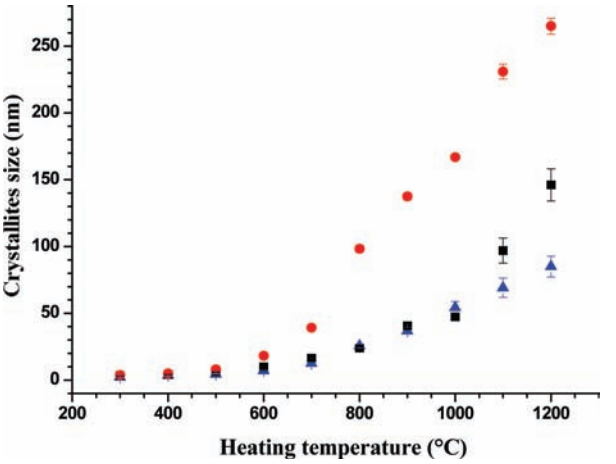

Figure 3. Variation of the average crystallite size versus the heating temperature obtained for CeO_2 (red circle), $Ce_{0.91}Nd_{0.09}O_{1.955}$ (black square), and $Ce_{0.84}Nd_{0.16}O_{1.92}$ (blue triangle) samples.

3.2. Structural and Microstructural Characterization. To evaluate the influence of the crystallization state on the behavior of $Ce_{1-x}Nd_xO_{2-x/2}$ samples during leaching tests, the structural (and microstructural) characterization of the powdered samples versus heating temperature was undertaken in terms of crystallization state (XRD), morphology (SEM), and specific surface area (N_2 adsorption-BET method).

XRD characterization. The $Ce_{2-2x}Ln_{2x}(C_2O_4)_3 \cdot 10H_2O$ precursors were thus heated each 100 °C from 200 to 1200 °C, then characterized by XRD (Figure 2). At 200 °C, the XRD patterns did not evidence any XRD lines, showing that the samples were fully amorphous. This observation was correlated to the full dehydration of the initial hydrated oxalates, as shown from DTA and TGA experiments. It appeared in good agreement with the results of Balboul et al. on the amorphous nature of $Nd_2(C_2O_4)_3$.[64] All the XRD lines characteristic of the fluorite-type structure adopted by $Ce_{1-x}Nd_xO_{2-x/2}$ mixed dioxides for $x < 0.4$[62,65] were then observed above 300 °C.[66] Moreover, no additional phase was detected, showing that trivalent neodymium was inserted in the structure in the cerium(IV) site, leading to the formation of $Ce_{1-x}Nd_xO_{2-x/2}$ solid solutions.[67] As already described in the literature, this substitution was associated with the formation of oxygen vacancies to ensure the charge compensation.[62,68,69] From 300 to 600 °C, the XRD lines remained broad and indicated that the crystallization state was not optimal. On the contrary, it was clearly improved between 700 and 1200 °C (where the XRD lines were found to be strongly narrowed). The associated refined unit cell parameters of CeO_2, $Ce_{0.91}Nd_{0.09}O_{1.955}$, and $Ce_{0.84}Nd_{0.16}O_{1.92}$ reached a = 5.4107(2), 5.4305(4), and 5.4489(1) Å, respectively (Table 2). All these values were in good agreement with the literature (a = 5.41134(8) Å for CeO_2, a = 5.43022(8) Å for $Ce_{0.9}Nd_{0.1}O_{1.95}$, and a = 5.45084(11) Å for $Ce_{0.8}Nd_{0.2}O_{1.9}$[18,62]). This increase with the trivalent neodymium mole loading was consistent with the incorporation of the bigger Nd(III) ($^{VIII}r_{Nd^{3+}}$ = 1.109 Å) compared to Ce(IV) ($^{VIII}r_{Ce^{4+}}$ = 0.97 Å).

To follow more accurately the variation of the crystallization state of $Ce_{1-x}Nd_xO_{2-x/2}$ solid solutions versus the heating temperature, the average full width at half-maximum (FWHM) was determined from the seven more intense XRD lines for all the prepared samples and were compared to that of the corundum reference. As expected from the peak shapes, the FWHM value strongly decreased from 300 to 600 °C, then progressively stabilized for T > 800 °C. The crystallization state of CeO_2 was considered to be optimized above this temperature.

In a second step, the application of the Rietveld method allowed determining the size of coherent domains (i.e., the average crystallite size) corresponding to the various crystallization states assumed from the FWHM values (Figure 3). Between 300 and 700 °C, they were found to vary from 5 to 40 nm (CeO_2) and from 5 to 15 nm ($Ce_{1-x}Nd_xO_{2-x/2}$), respectively. For higher temperatures, the crystallite size strongly increased: it reached 260, 140, and 80 nm for CeO_2, $Ce_{0.91}Nd_{0.09}O_{1.955}$, and $Ce_{0.84}Nd_{0.16}O_{1.92}$, respectively, when heating the samples at 1200 °C. This observation suggested a two-step process in the growth of crystallite size. It was first explained by the elimination of crystal defects and amorphous domains ($T \leq$ 700 °C), leading to the improvement of the crystallization state of the solid associated with a limited growth of the coherent domains. The second step, observed for temperatures higher than 800 °C, was mainly associated with the growth of crystallites through diffusion phenomena close to that responsible for sintering processes at the grain scale for higher temperatures. It suggested an Ostwald ripening process where small crystals were progressively integrated to form bigger ones that are stable at high temperatures.[70,71]

The important difference in the crystallite size observed between the three samples after heating at 1100 °C directly resulted from the influence of the neodymium incorporation in the structure. Such an effect was correlated to that observed during the DTA/TGA experiments from which a shift to the higher temperatures of all the chemical transformations (e.g., for the oxalate to oxide transformation) occurred when increasing the neodymium content in the structure. From the literature, this effect was mainly assigned to an heterogeneous distribution of neodymium in the sample. In this sense, Bellière et al. evidenced an enrichment in trivalent lanthanides within the grain boundaries and at the surface due to the space charge effect provoked by the lower charge of Ln^{3+} compared to that of Ce^{4+}.[72] They argued that the excess of trivalent cations located within the crystallite boundaries generated a gradient in concentration

dx.doi.org/10.1021/ic201269c |*Inorg. Chem.* 2011, 50, 9059–9072

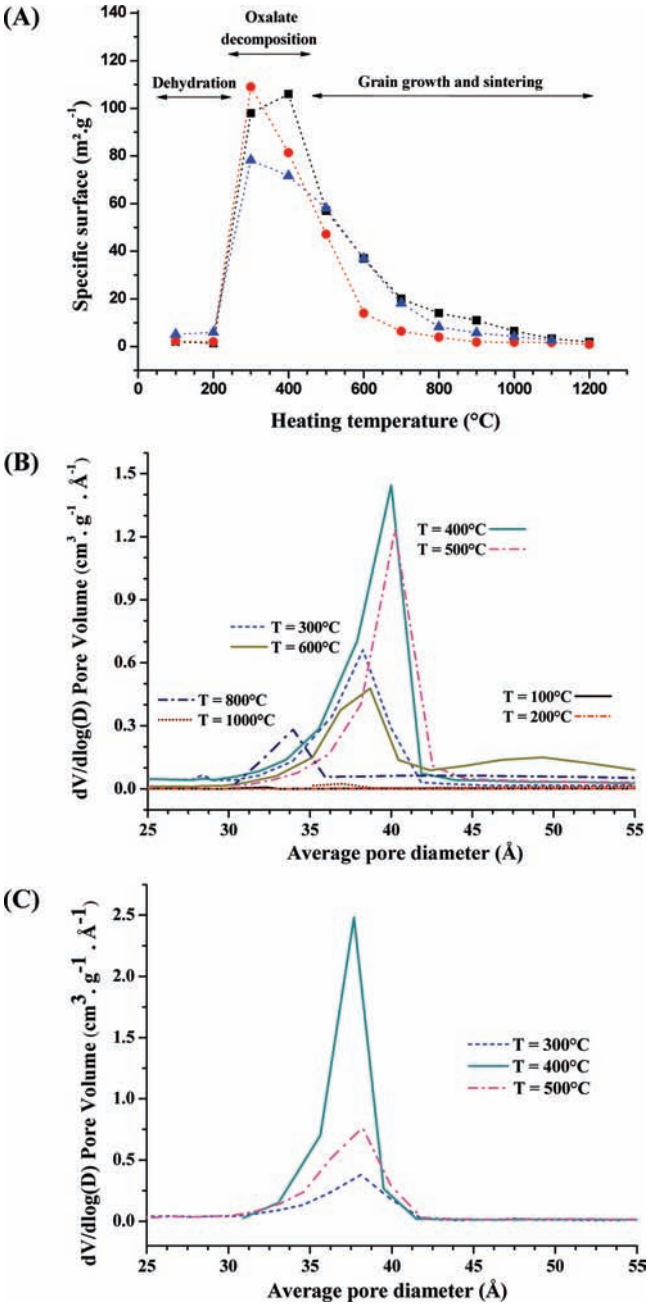

Figure 4. Variation of the specific surface area versus the heating temperature ($t = 2$ h) observed for CeO_2 (red circle), $Ce_{0.91}Nd_{0.09}O_{1.955}$ (black square), and $Ce_{0.84}Nd_{0.16}O_2$ (blue triangle) samples (A) and variation of the incremental pore area versus the average diameter of pores for $Ce_{0.91}Nd_{0.09}O_{1.955}$ heated at 100, 200, 300, 400, 500, 600, 800, and 1000 °C (B) and for $Ce_{0.84}Nd_{0.16}O_{1.92}$ heated at 300, 400, and 500 °C (C).

between the bulk and the surface, curbing the crystallite boundary migration and thus delaying the crystallites' growth.

The activation energy for the crystallite growth of CeO_2 and $Ce_{1-x}Nd_xO_{2-x/2}$, was estimated by eq 9[73]

$$D = k \times \exp\left(-\frac{E_{A,CG}}{R \times T}\right) \quad (9)$$

where k is a constant value, R the perfect gas constant, D the crystallite size, and $E_{A,CG}$ is the activation energy for crystallite growth. The plot of $\log(D)$ versus the reciprocal temperature led to an activation energy of 21 ± 2 kJ·mol^{-1} for the three compounds and for 700 °C ≤ T ≤ 1200 °C. Such a value was found to be independent of the chemical composition and was in good agreement with the experimental results obtained for nanopowdered samples of CeO_2 ($E_{A,CG}$ = 17 kJ·mol^{-1}).[74]

Morphological Characterization. The specific surface area of the prepared samples was followed versus the heating temperature (Figure 4A) and coupled to ESEM observations (Figure 5).

Whatever the sample studied, the specific surface area reached a maximum value higher than 80 m^2·g^{-1} when heating the samples between 300 and 400 °C. Such an increase was already reported by several authors for the decomposition of $Th_{1-x}U_x(C_2O_4)_2\cdot 2H_2O$[10] or $Ce_2(C_2O_4)_3\cdot 10H_2O$[75] oxalates. This increase was usually correlated to the dehydration of the samples, then to the decomposition of the oxalate entities into CO and CO_2, which induced the formation of defects (cracks, pores...) through the establishment of strong constraints associated with the release of large amounts of gaseous molecules. This range of temperatures was consistent with that expected from TGA and DTA experiments. Indeed, the oxalate-to-oxide transformation started at 300 and 350 °C for CeO_2 and $Ce_{1-x}Nd_xO_{2-x/2}$, respectively. Moreover, the observation of such a phase transformation and the subsequent formation of defects leading to the increase of the specific surface area was also correlated to the XRD data that revealed poorly crystallized samples in this range of temperatures.

Above this temperature, the specific surface area progressively decreased as a consequence of the improvement of the crystallization states of the samples and of crystallite growth processes. The decrease of the specific surface area was faster for CeO_2 than for $Ce_{1-x}Nd_xO_{2-x/2}$ (14 and 37 m^2·g^{-1}, respectively, for a heating temperature of 600 °C). This result was directly connected to the variation of the crystallinity of the resulting samples. At this temperature, the FWHM was twice larger for $Ce_{1-x}Nd_xO_{2-x/2}$ compared with CeO_2. This difference was kept up to 1000 °C, where the specific surface area decreased to 7 and 2 m^2·g^{-1} for $Ce_{0.91}Nd_{0.09}O_{1.955}$ and CeO_2, respectively. Simultaneously, the average crystallite size increased up to 40 nm ($Ce_{0.91}Nd_{0.09}O_{1.955}$) and 170 nm ($CeO_2$). Because the morphology of the powder was mainly conserved, such variations of the specific surface area were attributed to porosity modifications, consequently to the release of gaseous molecules during the oxalate conversion. Desorption isotherm analysis of $Ce_{0.91}Nd_{0.09}O_{1.955}$ and $Ce_{0.91}Nd_{0.09}O_{1.92}$ with the BJH method was thus performed in order to give additional information on the pore size distribution (Figure 4B,C). As expected from BET experiments, the modifications in the pore distribution were strongly affected by the heating temperature in the same way for both solid solutions. Indeed, the samples prepared at 400 °C exhibited nanometric porosity (with a pore size ranging from 3.5 to 4.5 nm) associated with ≈80% of the developed specific surface area. Because such nanometric porosity was not observed for the $Ce_{0.91}Nd_{0.09}O_{1.955}$ samples prepared at 100 and 200 °C, it was mainly associated with the decomposition of oxalate into oxide (and thus to the release of large amounts of gaseous molecules). For $Ce_{0.91}Nd_{0.09}O_{1.955}$, this pore size population remained observable up to 800 °C even if the associated surface area developed decreased significantly from 400 to 800 °C. Moreover, its relative contribution to the global surface remained predominant and almost constant (79−91% of S_{BET}) between both

dx.doi.org/10.1021/ic201269c |*Inorg. Chem.* 2011, 50, 9059–9072

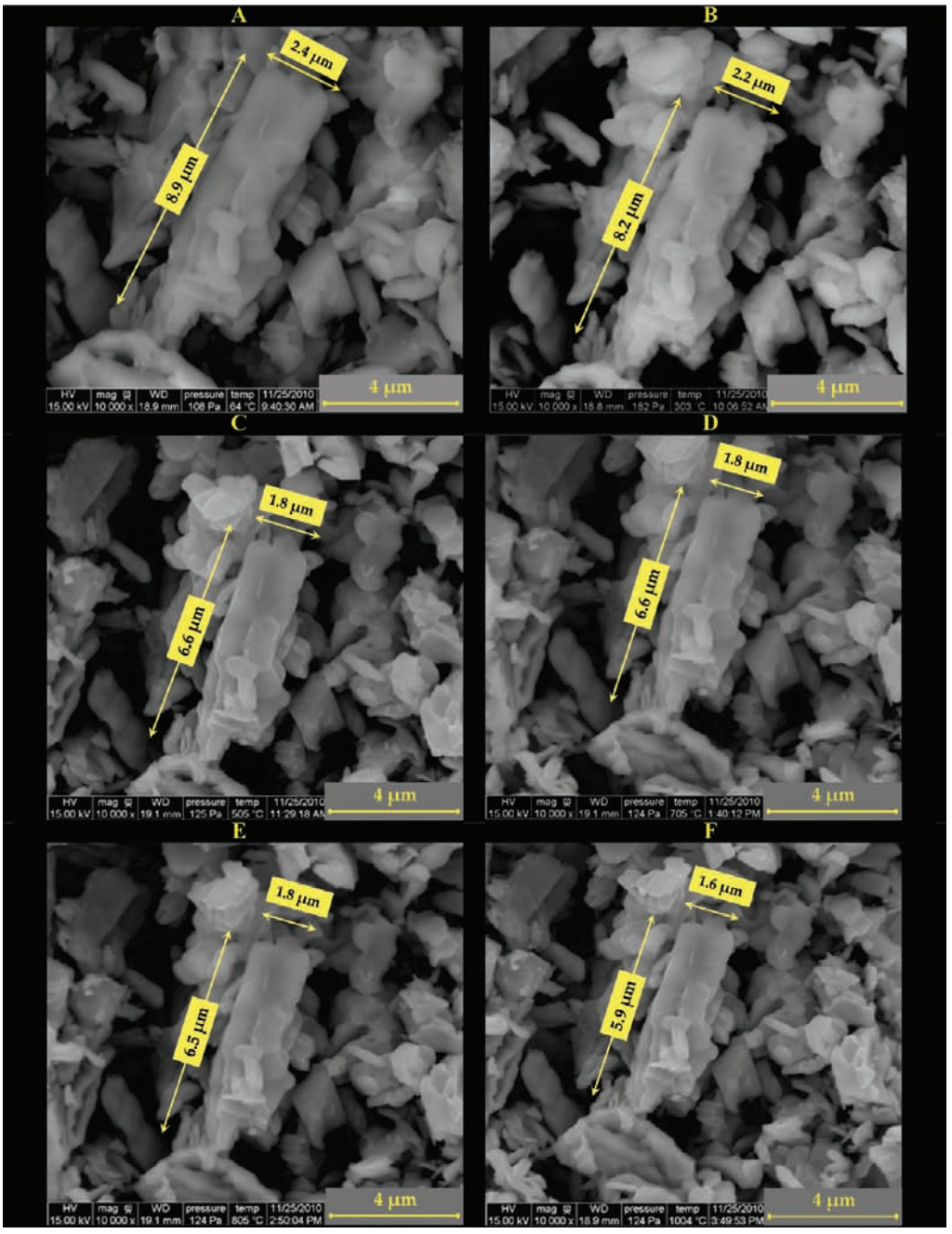

Figure 5. In situ HT-ESEM micrographs of the $Ce_2(C_2O_4)_3 \cdot 10H_2O$ starting precursor (A) and of resulting CeO_2 powders obtained after heating at 300 (B), 500 (C), 700 (D), 800 (E), and 1000 °C (F).

temperatures. After heating the $Ce_{0.91}Nd_{0.09}O_{1.955}$ samples at 1000 °C, this nanometric porosity was significantly reduced while the pore size increased up to 4.5−5.5 nm. This increase was mainly explained by the coalescence of nanometric pores simultaneous to the grain growth.

The decomposition of $Ce_2(C_2O_4)_3 \cdot 10H_2O$ was also followed in situ by HT-ESEM (Figure 5). ESEM micrographs showed that the samples were constituted by nanometric grains associated in lamellar-shaped aggregates of 2−10 μm in length. This morphology was kept all during the oxalate-to-oxide conversion (Figure 5A−C). However, the oxalate decomposition was characterized by an isotropic contraction of the aggregate size between 90 and 500 °C. This decrease in size of about 25% was mainly associated with the release of gaseous H_2O, CO, and CO_2 during the oxalate-to-oxide transformation. The grain sizes remained almost constant between 500 and 800 °C.

However, these micrographs did not explain the strong variations of surface area between 200 and 800 °C because the pores were too small (around 4 nm) to be highlighted unambiguously. At 1000 °C, the size of the aggregate was 5.9 μm in length and was 1.6 μm in width; this further decrease was explained by the beginning of the sintering of the powder.

3.3. Dissolution of CeO_2 and $Ce_{1-x}Nd_xO_{2-x/2}$ Samples. As already mentioned, the chemical durability of $Ce_{1-x}Nd_xO_{2-x/2}$

dx.doi.org/10.1021/ic201269c |*Inorg. Chem.* 2011, 50, 9059–9072

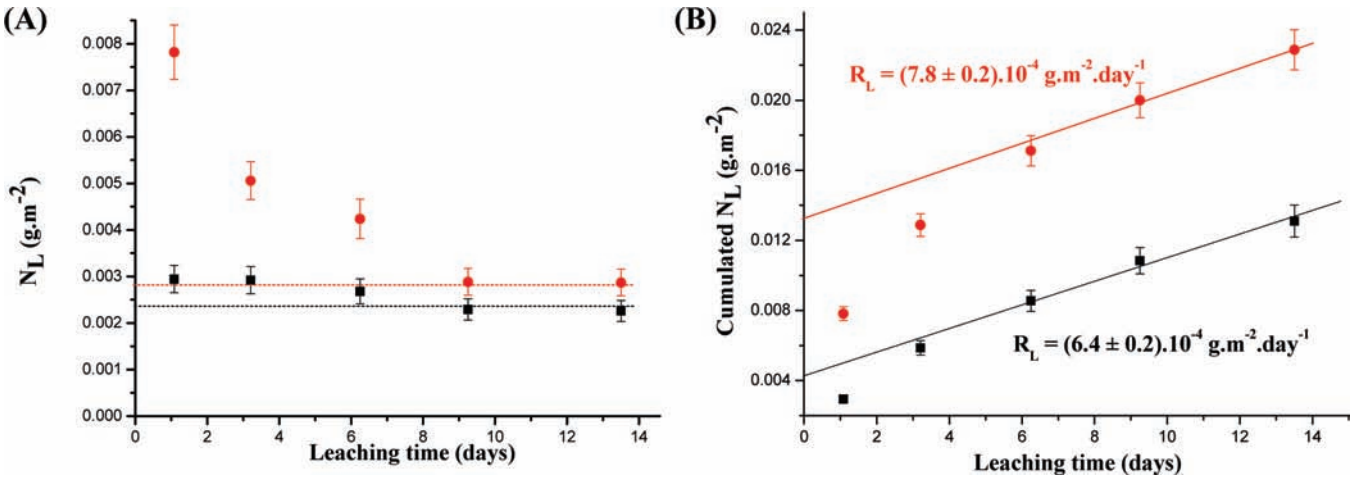

Figure 6. Evolution of the normalized leaching (A) and of the cumulative normalized leaching (B) during leaching tests of $Ce_{0.91}Nd_{0.09}O_{1.955}$ (fired at 1000 °C) in dynamic conditions (2 M HNO_3, T = 90 °C): N_L(Ce) (black square) and N_L(Nd) (red circle).

samples prepared at 1000 °C was examined through leaching tests performed in 2 M HNO_3 at 90 °C with a leachate renewal of 1 mL·h^{-1} (called "dynamic" experiments) to avoid the presence of saturation processes (Figure 6A,B). This kind of experiment also allowed evaluating the initial normalized dissolution rates (see section 2.3).[41,47,48,76] The evolution of the instantaneous normalized leachings N_L(Nd) and N_L(Ce) revealed a slight preferential release of neodymium during the first days of leaching that could reflect some differences in the energy of cohesion of both trivalent neodymium and tetravalent cerium within the samples. However, this phenomenon was mainly observed during the first days of leaching when using dynamic conditions. It was directly connected to the enrichment in trivalent lanthanide within the grain boundaries and at the surface of the samples already reported by Bellière et al.[72] Indeed, on the basis of this surface enrichment in neodymium compared to the bulk composition, the associated normalized dissolution rates were expected to be higher and thus would be directly correlated to this small difference between both elements during the first days of leaching time. On the basis of the direct comparison of both lanthanides, this initial pulse was always lower than 5% and 1% of initial neodymium and cerium contents, respectively. Consequently, the stoichiometric ratio f_i was affected by less than 3.3%, supporting the assumption made on its constancy (eqs 4 and 5).

As clearly shown in Figure 6A, the difference between both elements (through the determination of the N_L(Nd)/N_L(Ce) ratio) decreased when increasing the leaching time. Consequently, the final corresponding cumulative normalized leachings N_L(Nd) and N_L(Ce) varied linearly with rather similar slopes (Figure 6B). The initial $R_{L,0}$(Nd)/$R_{L,0}$(Ce) ratio was initially equal to 2.7 during the first day of leaching, then decreased down to 1.3 after 6 days, where the associated normalized dissolution rates $R_{L,0}$(Ce) and $R_{L,0}$(Nd) reached $(6.4 \pm 0.2) \times 10^{-4}$ and $(7.8 \pm 0.2) \times 10^{-4}$ g·m^{-2}·d^{-1}, respectively. Despite this initial release, the dissolution was rapidly found to be congruent. This point was confirmed for all the other leaching conditions examined. Even if the release of both elements was followed, the general trends of the normalized dissolution rate variation were privileged on cerium since (1) it was the major component of the leached samples and (2) the very slow normalized dissolution rates determined led to higher uncertainties associated with the neodymium concentration compared to that of cerium.

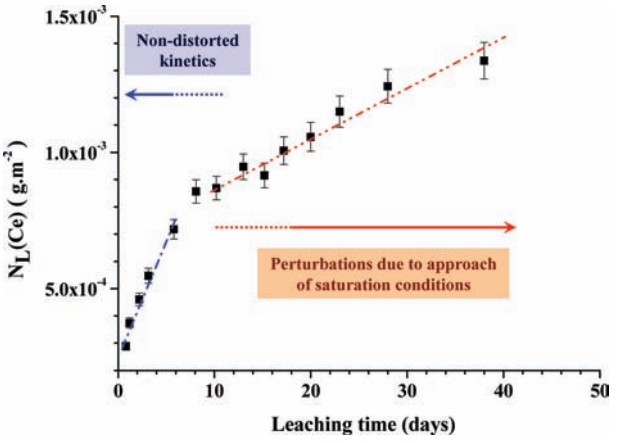

Figure 7. Evolution of the normalized leaching during leaching tests of $Ce_{0.91}Nd_{0.09}O_{1.955}$ (fired at 1000 °C) in static conditions (C) (2 M HNO_3, T = 60 °C): N_L(Ce) (black square) showing the two trends (far and near saturation conditions) usually observed during the dissolution of ceramic materials.[41,42,47,48].

To evidence the effect of several parameters, such as nitric acid concentration, leaching temperature, and crystallization state, the dissolution of samples was also studied with low leachate renewals (called "static" experiments). This kind of experiment allowed determining the initial normalized dissolution rates first, then studying the establishment of saturation processes (see section 2.3).[42] The variation of the normalized weight loss, N_L(Ce), determined when leaching $Ce_{0.91}Nd_{0.09}O_{1.955}$ (initially fired at 1000 °C) in 2 M HNO_3 at 60 °C is presented, as an example, in Figure 7. The general evolution of N_L(Ce) versus the leaching time clearly exhibited two tendencies. The first one, which is kinetically controlled, was observed before 10 days of leaching time. This linear variation allowed determining the initial normalized dissolution rate ($R_{L,0}$(Ce) = $(1.1 \pm 0.2) \times 10^{-4}$ g·m^{-2}·d^{-1}). It was followed by a significant slope drop that was usually assumed to be partly affected by the approach of saturation conditions, allowing the determination of the

Table 4. Initial Normalized Dissolution Rates $R_{L,0}$(Ce) and $R_{L,0}$(Nd) ($g \cdot m^{-2} \cdot d^{-1}$) Obtained during Leaching Tests of $Ce_{0.91}Nd_{0.09}O_{1.955}$ and CeO_2 (Fired at 1000 °C) Performed at 60 °C in Various Nitric Acid Leaching Solutions

compound		10^{-1} M HNO_3	5×10^{-1} M HNO_3	2 M HNO_3	6 M HNO_3
CeO_2	$R_{L,0}$(Ce)	$(3.2 \pm 0.2) \times 10^{-6}$	$(8.6 \pm 0.3) \times 10^{-6}$	$(2.9 \pm 0.3) \times 10^{-5}$	$(3.3 \pm 0.4) \times 10^{-5}$
$Ce_{0.91}Nd_{0.09}O_{1.955}$	$R_{L,0}$(Ce)	$(4.1 \pm 0.2) \times 10^{-6}$	$(3.9 \pm 0.3) \times 10^{-5}$	$(1.8 \pm 0.2) \times 10^{-4}$	$(3.1 \pm 0.2) \times 10^{-4}$
	$R_{L,0}$(Nd)	$(1.0 \pm 0.9) \times 10^{-5}$	$(2.0 \pm 1.0) \times 10^{-5}$	$(3 \pm 2) \times 10^{-4}$	$(8 \pm 2) \times 10^{-4}$

normalized dissolution rates near the establishment of thermodynamic equilibria ($R_{L,t}$(Ce) = $(1.7 \pm 0.2) \times 10^{-5}$ $g \cdot m^{-2} \cdot d^{-1}$).

Influence of the Nitric Acid Concentration. To underline the influence of nitric acid concentration on the normalized dissolution rates, some leaching tests were performed in various media (10^{-1}, 5×10^{-1}, 2, and 6 M HNO_3). The initial normalized dissolution rates $R_{L,0}$(Ce) and $R_{L,0}$(Nd) are gathered in Table 4, while the variations of log R_L(Ce) versus the leachate acidity are plotted in Figure 8 for $Ce_{0.91}Nd_{0.09}O_{1.955}$ and CeO_2 (fired at 1000 °C). For all the media studied, the normalized dissolution rates obtained when leaching CeO_2 were very slow (from $R_{L,0}$(Ce) = $(3.2 \pm 0.2) \times 10^{-6}$ $g \cdot m^{-2} \cdot d^{-1}$ to $R_{L,0}$(Ce) = $(3.3 \pm 0.4) \times 10^{-5}$ $g \cdot m^{-2} \cdot d^{-1}$). Such values confirmed the high chemical durability of this material during leaching or dissolution experiments, as already described for powdered and sintered ThO_2 samples ($R_{L,0}$(Th) = $(1.7 \pm 0.1) \times 10^{-7}$ $g \cdot m^{-2} \cdot d^{-1}$ when leaching the samples in 5 M HNO_3 at T = 25 °C[47]). It also suggested that no reduction of Ce(IV) into Ce(III) occurred during the dissolution processes. Moreover, the behavior of the samples was strongly affected by the nitric acid concentration, as already described for ThO_2 and $Th_{1-x}U_xO_2$ samples.[47,48] Indeed, an increase of 1 order of magnitude was obtained between 10^{-1} M HNO_3 and 2 M HNO_3 for CeO_2 ($R_{L,0}$(Ce) = $(3.2 \pm 0.2) \times 10^{-6}$ and $(2.9 \pm 0.4) \times 10^{-5}$ $g \cdot m^{-2} \cdot d^{-1}$, respectively) and almost 2 orders of magnitude for $Ce_{0.91}Nd_{0.09}O_{1.955}$ ($R_{L,0}$(Ce) = $(4.1 \pm 0.2) \times 10^{-6}$ and $(1.8 \pm 0.2) \times 10^{-4}$ $g \cdot m^{-2} \cdot d^{-1}$, respectively). From these results, the behavior of the $Ce_{0.91}Nd_{0.09}O_{1.955}$ solid solution was thus more affected than CeO_2 by the increase of nitric acid concentration. This difference surely resulted from the presence of oxygen vacancies in the mixed cerium−neodymium oxide that led to a weakening of the crystal lattice and thus to a decrease of the chemical durability of the leached samples.[62]

Moreover, as described by Lasaga,[39] the normalized dissolution rate should increase linearly with the logarithm of the proton activity at the solid−solution interface. That was observed for the major part of the nitric acid solutions considered. However, we observed a decrease of the influence of nitric acid concentration for 6 M HNO_3 (Figure 8). In such conditions, increasing the nitric acid concentration probably led to the progressive saturation of active sites present at the surface of the samples that reduced significantly the effect of protons in this range of concentration.

As expected from eq 7, the linear variation of log($R_{L,0}$) versus log(H_3O^+) allowed determining the partial order related to the proton activity, n, for both CeO_2 and $Ce_{0.91}Nd_{0.09}O_{1.955}$ samples. The free proton concentrations were determined according to the literature.[77,78] The fractional dependence with proton activity was usually interpreted in several ways according to the authors. The study of Al_2O_3 and BeO dissolutions already evidenced that the partial order related to the protons activity was equal to the charge of the central cation.[51] However, the study of the dissolution of $NaAlSi_3O_8$ showed that the n value was independent of the central charge of the cation.[52] The authors suggested that this partial order could be directly connected to the number of protons adsorbed onto the surface of the leached samples and thus to the concentration of active sites at the solid/liquid interface.

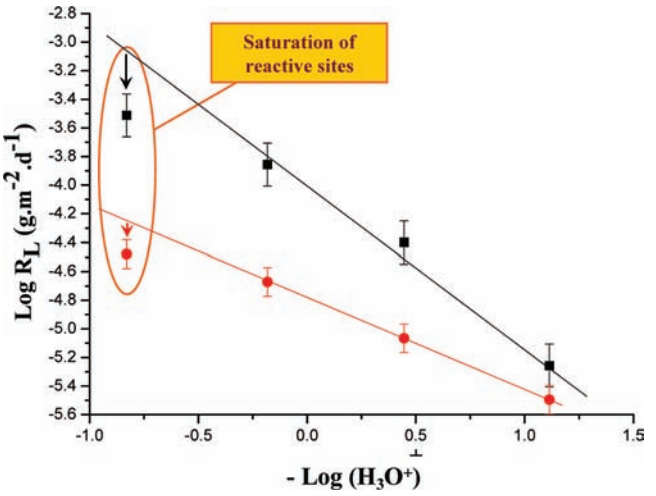

Figure 8. Variation of log($R_{L,0}$(Ce)) versus the opposite log(H_3O^+) during leaching tests of $Ce_{0.91}Nd_{0.09}O_{1.955}$ (black square) and CeO_2 (red circle) in various HNO_3 solutions (T = 60 °C).

From the cerium releases, the n values reached 0.63 ± 0.05 for CeO_2 and 1.1 ± 0.1 for $Ce_{0.91}Nd_{0.09}O_{1.955}$, showing different behaviors for the two solids during leaching tests. In the case of $Ce_{0.91}Nd_{0.09}O_{1.955}$, the n value was in good agreement with that determined from the neodymium releases (1.1 ± 0.3) despite a high associated uncertainty mainly due to the low concentrations of neodymium measured in the leachate. The value obtained for CeO_2 was consistent with that reported for the other materials and minerals, including the refractory ThO_2 (Table 3). Because $n > 1$ for $Ce_{0.91}Nd_{0.09}O_{1.955}$, the dissolution of $Ce_{1-x}Nd_xO_{2-x/2}$ solid solutions may be mainly governed by the presence of oxygen vacancies (and, consequently, strongly affected by the decrease of the energy of cohesion), associated with the incorporation of a trivalent element in the structure instead of by the adsorption of active species onto the surface of the sample. Indeed, the rates associated with the elementary releases from these solids would be significantly higher than that of adsorption species at the solid/liquid interface. The same conclusions were made for uranium-enriched $Th_{1-x}U_xO_2$ solid solutions when comparing the uranium oxidation rate with that of detachment of species from the solid by complexion.[48] The chemical durability of $Ce_{1-x}Nd_xO_{2-x/2}$ solid solutions would be strongly affected by the M(IV)/M(III) cationic substitution when increasing the neodymium content.[62]

Influence of the Temperature. As already discussed, temperature is also a key parameter affecting the behavior of samples

dx.doi.org/10.1021/ic201269c |*Inorg. Chem.* 2011, 50, 9059–9072

during dissolution. During leaching experiments of CeO_2 in 2 M HNO_3, the normalized dissolution rate was increased by a factor of 2 when increasing the leaching temperature from 60 °C ($R_{L,0}(Ce) = (2.9 \pm 0.3) \times 10^{-5}$ g·m^{-2}·d^{-1}) to 90 °C ($R_{L,0}(Ce) = (5.5 \pm 0.4) \times 10^{-5}$ g·m^{-2}·d^{-1}). For $Ce_{0.91}Nd_{0.09}O_{1.955}$, the increasing factor was equal to 2.5 ($R_{L,0}(Ce) = (1.8 \pm 0.2) \times 10^{-4}$ g·m^{-2}·d^{-1} for $T = 60$ °C and $(4.5 \pm 0.2) \times 10^{-4}$ g·m^{-2}·d^{-1} for $T = 90$ °C). According to eq 7, the slopes obtained by linear regression when plotting $\log(R_{L,0})$ versus the reciprocal temperature for both CeO_2 and $Ce_{0.91}Nd_{0.09}O_{1.955}$ samples led to an apparent activation energy between 36 and 37 kJ mol^{-1}. Such values were consistent with the control of the dissolution by surface reactions occurring at the solid/liquid interface, as already described in the literature,[38,39,47,52] and were too high to consider that only diffusion phenomena controlled the dissolution (since $E_A > 20$ kJ mol^{-1}).[79]

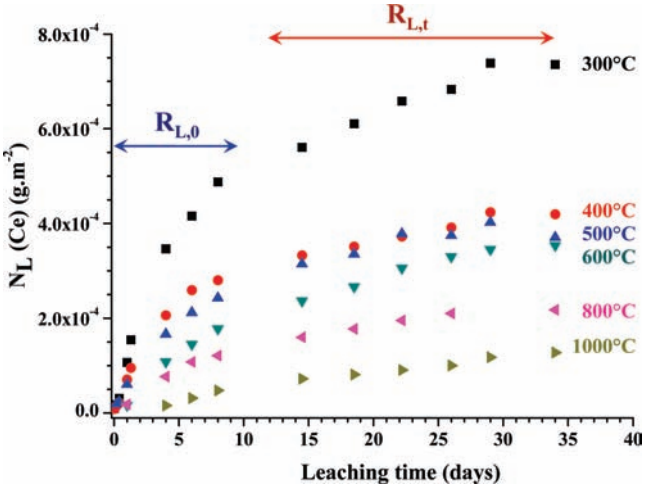

Figure 9. Evolution of the normalized leachings $N_L(Ce)$ obtained during the dissolution of powdered CeO_2 samples (2 M HNO_3, $T = 60$ °C) prepared for various temperatures of heating treatment.

Influence of the Crystallization State. Some rare and recent publications dealt with the study of discrepancies observed in the ThO_2 solubility.[80] They mainly underlined a lack of thorough solid-state analysis and pointed out the role of specific site exchange mechanisms at the solid/liquid interface through experiments based on isotopic exchanges. However, the studies devoted to the links observed between physicochemical properties of the samples and their behavior during leaching tests were rarely considered,[7] while they probably exhibited an important contribution on the normalized dissolution rates. For this reason, the effect of additional parameters on the normalized dissolution rates, such as the crystallization state of the samples, was also examined. The chemical durability of powdered CeO_2, $Ce_{0.91}Nd_{0.09}O_{1.955}$, and $Ce_{0.84}Nd_{0.16}O_{1.92}$ samples with various crystallization states was studied in 2 M HNO_3 at 60 °C. For instance, the evolution of the normalized weight loss, $N_L(Ce)$, obtained when leaching powdered CeO_2 samples heated at various temperatures between 300 and 1000 °C, is gathered in Figure 9. For the three chemical compositions examined, the resulting initial normalized dissolution rates $R_{L,0}(Ce)$ and $R_{L,0}(Nd)$ are gathered in Table 5, while the variations of $R_{L,0}(Ce)$ versus the temperature of heating treatment are reported, as an example, in Figure 10. For all the heating temperatures considered, the more important the neodymium content in the solid solution, the more rapid the normalized dissolution rate, as the proof of the important role of oxygen vacancies on the chemical durability of the samples.

Despite the normalization of the elementary releases by the mass ratios (f_i) and by the reactive surface area (S) associated with the solid/liquid interface (see eqs 3 and 4), the initial normalized dissolution rates, $R_{L,0}(Ce)$ and $R_{L,0}(Nd)$, decreased

Table 5. Initial Normalized Dissolution Rates $R_{L,0}(Ce)$ and $R_{L,0}(Nd)$ (Expressed in g·m^{-2}·d^{-1}) Obtained during the Dissolution of CeO_2, $Ce_{0.91}Nd_{0.09}O_{1.955}$, and $Ce_{0.84}Nd_{0.16}O_{1.92}$ for Several Calcination Temperatures (2M HNO_3, $T = 60$ °C)

heating temperature		300 °C	400 °C	500 °C	600 °C
CeO_2	$R_{L,0}(Ce)$	$(1.1 \pm 1) \times 10^{-4}$	$(6.7 \pm 1.5) \times 10^{-5}$	$(5.1 \pm 1.2) \times 10^{-5}$	$(5.0 \pm 1.1) \times 10^{-5}$
$Ce_{0.91}Nd_{0.09}O_{1.955}$	$R_{L,0}(Ce)$	$(5.1 \pm 0.2) \times 10^{-4}$	$(4.1 \pm 0.3) \times 10^{-4}$	$(2.3 \pm 0.2) \times 10^{-4}$	$(1.6 \pm 0.2) \times 10^{-4}$
	$R_{L,0}(Nd)$	$(1.2 \pm 0.1) \times 10^{-3}$	$(9.3 \pm 0.9) \times 10^{-4}$	$(6.9 \pm 0.9) \times 10^{-4}$	$(4.1 \pm 0.5) \times 10^{-4}$
$Ce_{0.84}Nd_{0.16}O_{1.92}$	$R_{L,0}(Ce)$	$(1.2 \pm 0.1) \times 10^{-3}$	$(9.3 \pm 0.7) \times 10^{-4}$	$(6.0 \pm 0.8) \times 10^{-4}$	$(7.0 \pm 0.5) \times 10^{-4}$
	$R_{L,0}(Nd)$	$(2.5 \pm 0.3) \times 10^{-3}$	$(2.4 \pm 0.3) \times 10^{-3}$	$(1.3 \pm 0.2) \times 10^{-3}$	$(6.2 \pm 0.5) \times 10^{-4}$
heating temperature		700 °C	800 °C	900 °C	
CeO_2	$R_{L,0}(Ce)$	$(2.6 \pm 1.5) \times 10^{-5}$	$(1.8 \pm 1.1) \times 10^{-5}$	$(2.7 \pm 1.2) \times 10^{-5}$	
$Ce_{0.91}Nd_{0.09}O_{1.955}$	$R_{L,0}(Ce)$	$(1.1 \pm 0.3) \times 10^{-4}$	$(6 \pm 2) \times 10^{-5}$	$(5 \pm 3) \times 10^{-5}$	
	$R_{L,0}(Nd)$	$(3.1 \pm 0.8) \times 10^{-4}$	$(1.2 \pm 0.1) \times 10^{-4}$	$(1.1 \pm 0.3) \times 10^{-4}$	
$Ce_{0.84}Nd_{0.16}O_{1.92}$	$R_{L,0}(Ce)$	$(5.9 \pm 0.6) \times 10^{-4}$	$(4.7 \pm 0.4) \times 10^{-4}$	$(5.2 \pm 0.4) \times 10^{-4}$	
	$R_{L,0}(Nd)$	$(1.0 \pm 0.2) \times 10^{-3}$	$(8.7 \pm 1.0) \times 10^{-4}$	$(1.3 \pm 0.2) \times 10^{-3}$	
heating temperature		1000 °C	1100 °C	1200 °C	
CeO_2	$R_{L,0}(Ce)$	$(8 \pm 6) \times 10^{-6}$	$(6 \pm 3) \times 10^{-6}$	$(1.4 \pm 0.3) \times 10^{-5}$	
$Ce_{0.91}Nd_{0.09}O_{1.955}$	$R_{L,0}(Ce)$	$(7 \pm 2) \times 10^{-5}$	$(6 \pm 2) \times 10^{-5}$	$(6 \pm 2) \times 10^{-5}$	
	$R_{L,0}(Nd)$	$(1.2 \pm 0.2) \times 10^{-4}$	$(1.3 \pm 0.2) \times 10^{-4}$	$(2.2 \pm 0.4) \times 10^{-4}$	
$Ce_{0.84}Nd_{0.16}O_{1.92}$	$R_{L,0}(Ce)$	$(4.8 \pm 0.3) \times 10^{-4}$	$(1.6 \pm 0.9) \times 10^{-4}$	ND	
	$R_{L,0}(Nd)$	$(9.1 \pm 1.0) \times 10^{-4}$	$(5.7 \pm 0.6) \times 10^{-4}$	ND	

ND: not determined.

dx.doi.org/10.1021/ic201269c |*Inorg. Chem.* 2011, 50, 9059–9072

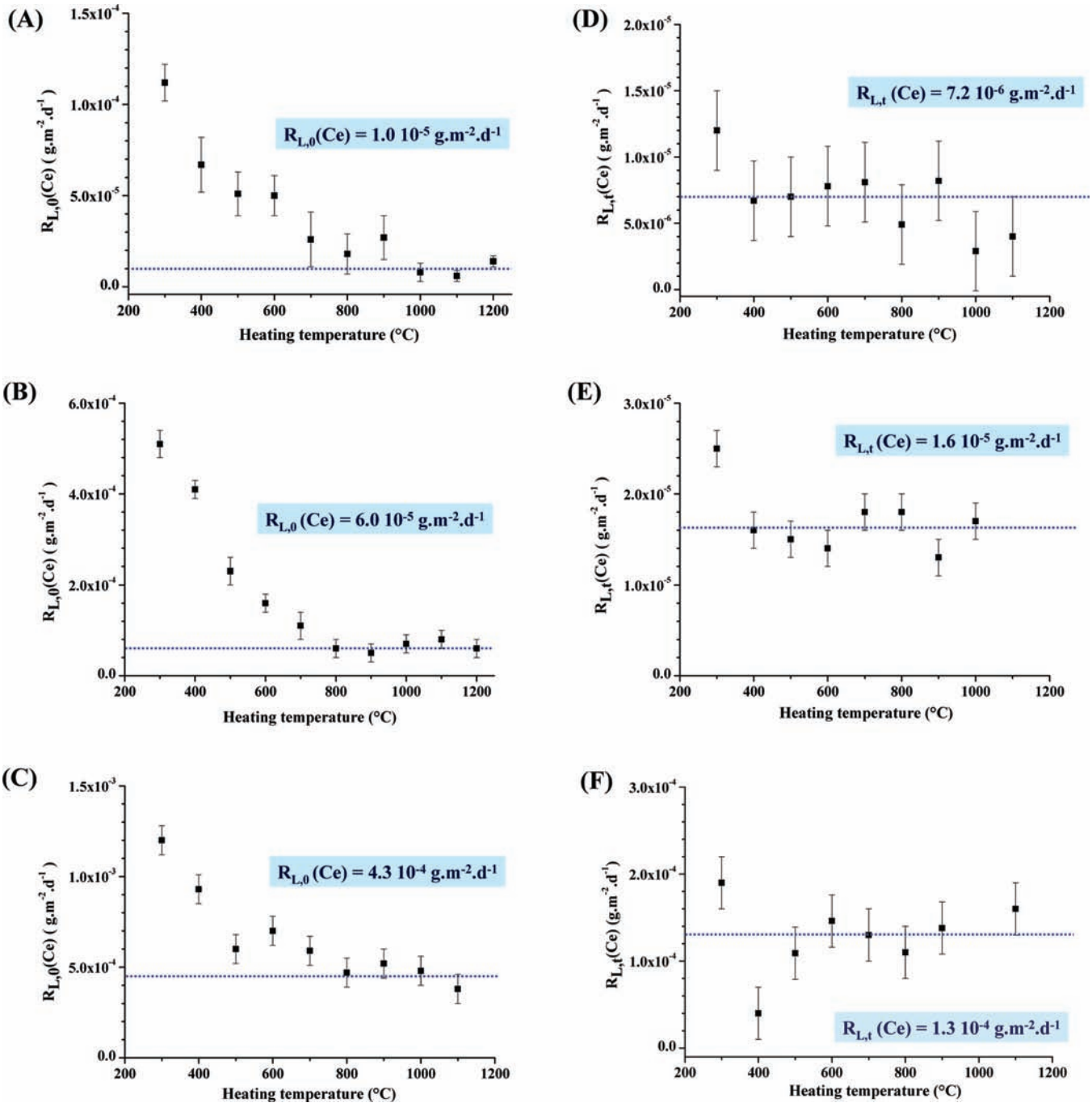

Figure 10. Variation of the initial normalized dissolution rate $R_{L,0}$(Ce) of CeO_2 (A), of $Ce_{0.91}Nd_{0.09}O_{1.955}$ (B), and of $Ce_{0.84}Nd_{0.16}O_2$ (C) and of the long-term normalized dissolution rate $R_{L,t}$(Ce) of CeO_2 (D), of $Ce_{0.91}Nd_{0.09}O_{1.955}$ (E), and of $Ce_{0.84}Nd_{0.16}O_2$ (F) versus the firing temperature (2 M HNO_3, T = 60 °C).

significantly from 300 to 800 °C for the three compositions examined. For instance, the $R_{L,0}$(Ce) values reached (5.1 ± 0.2) × 10^{-4} and (6 ± 2) × 10^{-5} g·m^{-2}·d^{-1} when leaching powdered $Ce_{0.91}Nd_{0.09}O_{1.955}$ samples initially prepared at 300 and 800 °C, respectively. For CeO_2 and $Ce_{0.91}Nd_{0.09}O_{1.955}$, the initial normalized dissolution rate was divided by a factor of 6.1 to 8.5 when increasing the firing temperature from 300 to 800 °C. This factor was less important for $Ce_{0.84}Nd_{0.16}O_{1.92}$, probably due to the higher normalized dissolution rates determined. Above 800 °C, the normalized dissolution rate values were almost stabilized.

This two-step variation of the initial normalized dissolution rate with the heating temperature was directly connected to that observed for the crystallite growth. Indeed, in the first temperature range (300 °C < T < 800 °C), mainly associated with the elimination of crystal defects and of amorphous domains, the improvement of the crystallization state played an important role on the normalized dissolution rate. Once again, such an effect was probably linked to the decrease of the energy of cohesion and, consequently, to the presence of such crystal defects.

dx.doi.org/10.1021/ic201269c |*Inorg. Chem.* 2011, 50, 9059–9072

Table 6. Long-Term Normalized Dissolution Rates $R_{L,t}$(Ce) and $R_{L,t}$(Nd) (Expressed in $g \cdot m^{-2} \cdot d^{-1}$) Obtained during the Dissolution of CeO_2, $Ce_{0.91}Nd_{0.09}O_{1.955}$, and $Ce_{0.84}Nd_{0.16}O_{1.92}$ for Several Calcination Temperatures (2M HNO_3, T = 60 °C)

heating temperature		300 °C	400 °C	500 °C
CeO_2	$R_{L,t}$(Ce)	$(1.2 \pm 0.3) \times 10^{-5}$	$(7 \pm 3) \times 10^{-6}$	$(7 \pm 3) \times 10^{-6}$
$Ce_{0.91}Nd_{0.09}O_{1.955}$	$R_{L,t}$(Ce)	$(2.5 \pm 0.2) \times 10^{-5}$	$(1.6 \pm 0.2) \times 10^{-5}$	$(1.5 \pm 0.2) \times 10^{-5}$
	$R_{L,t}$(Nd)	$(1.1 \pm 0.4) \times 10^{-5}$	$(1.3 \pm 0.1) \times 10^{-5}$	$(9.0 \pm 4.0) \times 10^{-6}$
$Ce_{0.84}Nd_{0.16}O_{1.92}$	$R_{L,t}$(Ce)	$(1.9 \pm 0.3) \times 10^{-4}$	$(4.0 \pm 0.3) \times 10^{-5}$	$(1.1 \pm 0.3) \times 10^{-4}$
	$R_{L,t}$(Nd)	ND	ND	ND
heating temperature		600 °C	700 °C	800 °C
CeO_2	$R_{L,t}$(Ce)	$(8 \pm 3) \times 10^{-6}$	$(8 \pm 3) \times 10^{-6}$	$(5 \pm 3) \times 10^{-6}$
$Ce_{0.91}Nd_{0.09}O_{1.955}$	$R_{L,t}$(Ce)	$(1.4 \pm 0.2) \times 10^{-5}$	$(1.8 \pm 0.2) \times 10^{-5}$	$(1.8 \pm 0.2) \times 10^{-5}$
	$R_{L,t}$(Nd)	$(8.8 \pm 5.0) \times 10^{-6}$	$(1.7 \pm 0.2) \times 10^{-5}$	$(1.6 \pm 0.2) \times 10^{-5}$
$Ce_{0.84}Nd_{0.16}O_{1.92}$	$R_{L,t}$(Ce)	$(1.5 \pm 0.3) \times 10^{-4}$	$(1.3 \pm 0.3) \times 10^{-4}$	$(1.1 \pm 0.3) \times 10^{-4}$
	$R_{L,t}$(Nd)	ND	ND	ND
heating temperature		900 °C	1000 °C	1100 °C
CeO_2	$R_{L,0}$(Ce)	$(8 \pm 3) \times 10^{-6}$	$(3 \pm 3) \times 10^{-6}$	$(4 \pm 3) \times 10^{-6}$
$Ce_{0.91}Nd_{0.09}O_{1.955}$	$R_{L,0}$(Ce)	$(1.3 \pm 0.2) \times 10^{-5}$	$(1.7 \pm 0.2) \times 10^{-5}$	$(2.9 \pm 0.2) \times 10^{-5}$
	$R_{L,0}$(Nd)	$(6.7 \pm 3.0) \times 10^{-6}$	$(3.7 \pm 0.8) \times 10^{-5}$	$(3.5 \pm 0.5) \times 10^{-5}$
$Ce_{0.84}Nd_{0.16}O_{1.92}$	$R_{L,0}$(Ce)	$(1.4 \pm 0.3) \times 10^{-5}$	ND	ND
	$R_{L,0}$(Nd)	ND[a]	ND[a]	ND[a]

[a] ND: not determined.

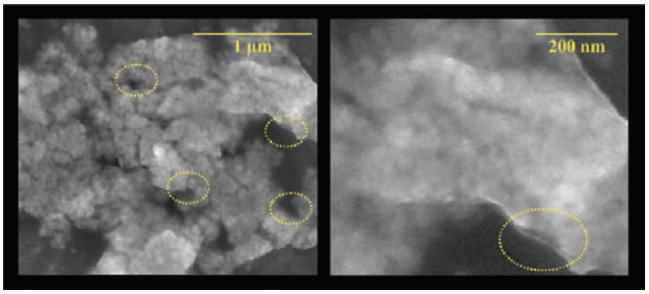

Figure 11. ESEM micrograph of the CeO_2 powdered sample leached for 2 months in 2 M HNO_3 showing the presence of a gelatinous layer at the surface of the crystallites (this layer was unstable under the electron beam).

On the contrary, increasing the heating temperature above this range (900 °C < T < 1200 °C) had no significant effect on the chemical durability of the powders. Because the initial normalized dissolution rates remained almost constant while the crystallite size was significantly increased, both parameters seemed to be independent.

Moreover, all the experiments performed using static conditions exhibited two tendencies, as already described. The decrease from the initial normalized dissolution rates, $R_{L,0}$, to the lower values obtained near saturation conditions, $R_{L,t}$, was observed for both cerium and neodymium, for all the samples, and all the firing temperatures. However, due to the higher reactive surface between the solid and the solution for the lower temperatures of calcination, the duration of the kinetics control was significantly reduced compared to the results obtained for samples heated at higher temperatures. The influence of the firing temperature on the long-term normalized dissolution rates was thus followed. These latter were significantly affected by the chemical composition of the prepared solid solution. Indeed, the average $R_{L,t}$ values reached 7.2 × 10^{-6} $g \cdot m^{-2} \cdot d^{-1}$ (Ce) for CeO_2, 1.6 × 10^{-5} $g \cdot m^{-2} \cdot d^{-1}$ (Ce) and 1.7 × 10^{-5} $g \cdot m^{-2} \cdot d^{-1}$ (Nd) for $Ce_{0.91}Nd_{0.09}O_{1.955}$, and 1.3 × 10^{-4} $g \cdot m^{-2} \cdot d^{-1}$ (Ce) for $Ce_{0.84}Nd_{0.16}O_{1.92}$ (Table 6, Figure 10). Conversely to what was noted for the initial normalized dissolution rates, the firing temperature had no effect on these long-term normalized dissolution rates despite the elimination of crystal defects then the increase of crystallite size. This result was mainly explained by the presence of a neoformed amorphous gelatinous layer formed onto the surface of the leached samples (Figure 11). As observed on ESEM micrographs, such a phase was found to form a 20 nm layer surrounding the initial grains. The complete characterization of such a phase that seemed to act as a diffusion barrier during the elementary releases is now under progress especially by making complementary leaching tests on well-densified CeO_2 and $Ce_{1-x}Nd_xO_{2-x/2}$ samples.

4. CONCLUSION

Several physicochemical properties of CeO_2 and $Ce^{IV}_{1-x}Nd^{III}_xO_{2-x/2}$ mixed oxides were studied in the field of their influence on their chemical durability. A summary of their effect on the normalized dissolution rates is reported in Figure 12. Some of them (temperature, acidity, chemical composition), whose influences were usually described in the literature for other materials, suggested that the dissolution was mainly driven by surface reactions occurring at the solid/liquid interface. Moreover, the incorporation of trivalent lanthanide in the fluorite structure strongly affected the chemical durability of such mixed oxides due to the correlated formation of oxygen vacancies. The effects of some others, such as crystal defects or crystallite size, were never discussed in the literature for oxide samples. Although the initial normalized dissolution rates slightly depended on the elimination of crystal defects for firing temperatures below 800 °C, they were mainly independent of the crystallite size

dx.doi.org/10.1021/ic201269c |Inorg. Chem. 2011, 50, 9059–9072

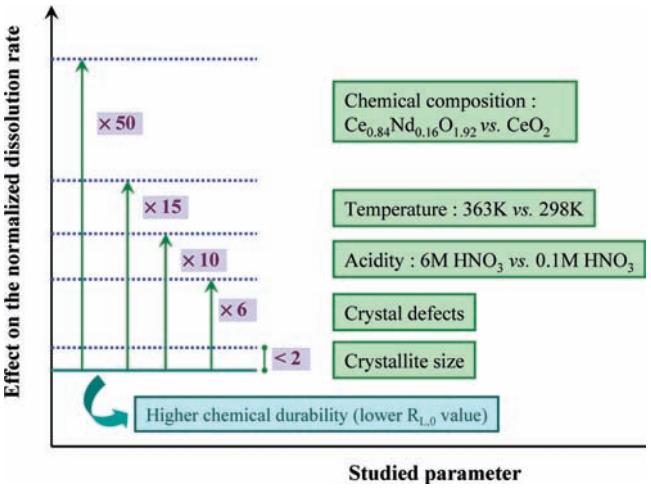

Figure 12. Influence of studied physicochemical parameters on the CeO_2 normalized dissolution rate.

($T \geq 900$ °C). Finally, near the establishment of thermodynamic equilibrium, the resulting normalized dissolution rates were less affected due to the formation of a gelatinous protective layer at the solid/liquid interface.

In order to complete this study, the effect of some other physicochemical parameters is now under progress. For instance, the correlations between variation of the densification rate observed when varying the operating conditions of $Ce^{IV}_{1-x}Nd^{III}_{x}O_{2-x/2}$ sintering and the chemical durability of the leached pellets are now under study.

Comparative leaching tests of $Ce^{IV}_{1-x}Nd^{III}_{x}O_{2-x/2}$ and $Th^{IV}_{1-x}Nd^{III}_{x}O_{2-x/2}$ are also under progress to confirm that no significant redox reaction involving the reduction of Ce(IV) into Ce(III) occurred during these dissolution experiments.

AUTHOR INFORMATION

Corresponding Author

*Phone: + 33 4 66 33 92 05. Fax: + 33 4 66 79 76 11. E-mail: nicolas.dacheux@univ-montp2.fr.

ACKNOWLEDGMENT

The authors would like to thank Adel Mesbah for his help in the refinement of XRD data. They also thank the MATINEX French Research Group (Innovative materials in extreme conditions, CEA/CNRS/AREVA/EDF/French Universities) included in the PACEN Program for their subsequent financial support. This work also benefited from the financial support of the French National Research Agency (ANR, project # ANR-08-BLAN-0216) and from the CNRS Interdisciplinary Research Program MaProSu (Matériaux et Procédés de Remplacement/Substitution).

REFERENCES

(1) Ichimiya, M.; Sagayama, Y. *Trans. Am. Nucl. Soc.* **2004**, *90*, 46–47.
(2) Hoffelner, W. *Chimia* **2005**, *59*, 977–982.
(3) Tommasi, J.; Delpech, M.; Groullier, J. P.; Zaetta, A. *Nucl. Technol.* **1995**, *111*, 133–148.
(4) Buisson, P. Ph.D. Thesis, GRE1-0519, University Grenoble 1, Grenoble, France, 1999.
(5) Arab-Chapelet, B.; Grandjean, S.; Nowogrocki, G.; Abraham, F. *J. Alloys Compd.* **2007**, *444*−*445*, 387–390.
(6) Matthews, R. B.; Davies, N. C. *OSTI Technical Report*, No. PNL3210; Office of Scientific and Technical Information, U.S. Department of Energy: Oak Ridge, TN, 1979.
(7) Hubert, S.; Barthelet, K.; Fourest, B.; Lagarde, G.; Dacheux, N.; Baglan, N. *J. Nucl. Mater.* **2001**, *297*, 206–213.
(8) Mitra, N. K.; Mahapatra, S. S.; Chattopadhyay, A. K. *J. Indian Chem. Soc.* **1983**, *60*, 499–501.
(9) Hingant, N.; Clavier, N.; Dacheux, N.; Barre, N.; Hubert, S.; Obbade, S.; Taborda, F.; Abraham, F. *J. Nucl. Mater.* **2009**, *385*, 400–406.
(10) Hingant, N.; Clavier, N.; Dacheux, N.; Hubert, S.; Barre, N.; Podor, R.; Aranda, L. *Powder Technol.* **2011**, *208*, 454–460.
(11) Oudinet, G.; Munoz-Viallard, I.; Aufore, L.; Gotta, M. J.; Becker, J. M.; Chiarelli, G.; Castelli, R. *J. Nucl. Mater.* **2008**, *375*, 86–94.
(12) Kim, H. S.; Joung, C. Y.; Lee, B. H.; Oh, J. Y.; Koo, Y. H.; Heimgartner, P. *J. Nucl. Mater.* **2008**, *378*, 98–104.
(13) Shannon, R. D. *Acta Crystallogr.* **1976**, *32*, 751–767.
(14) Lopez, C.; Deschanels, X.; Bart, J. M.; Boubals, J. M.; Den Auwer, C.; Simoni, E. *J. Nucl. Mater.* **2003**, *312*, 76–80.
(15) Cetiner, Z. S. *Environ. Monit. Assess.* **2009**, *151*, 279–287.
(16) Dacheux, N.; Clavier, N.; Robisson, A. C.; Terra, O.; Audubert, F.; Lartigue, J. E.; Guy, C. *C. R. Chim.* **2004**, *7*, 1141–1152.
(17) Terra, O.; Dacheux, N.; Audubert, F.; Podor, R. *J. Nucl. Mater.* **2006**, *352*, 224–232.
(18) Burghartz, M. *J. Alloys Compd.* **1998**, *271*−*273*, 544–548.
(19) Momin, A. C. *J. Nucl. Mater.* **1991**, *185*, 308–310.
(20) Tsuji, T. *J. Alloys Compd.* **1998**, *271*−*273*, 391–394.
(21) Taylor, D. *Trans. J. Br. Ceram. Soc.* **1984**, *83*, 32.
(22) Benedict, U. *Physica B+C* **1980**, *102*, 303–307.
(23) Fournier, S. Etude de la dissolution des oxydes mixtes $(U,Pu)O_2$ à forte teneur en plutonium. Ph.D. Thesis, No. 00 MON2 0203, Université Montpellier II, Montpellier, France, 2000.
(24) Nikitina, G. P.; Zhukova, I. N.; Egorova, V. P. *Radiochemistry* **1995**, *37*, 193–196.
(25) Uriarte, A. L.; Rainey, R. H. *Dissolution of high-density UO_2, PuO_2 and UO_2-PuO_2 pellets in inorganic acids*; Technical Report ORNL-3695; 1965; DOI: 10.2172/4652087.
(26) Juillet, F.; Adnet, J. M.; Gasgnier, M. *J. Radioanal. Nucl. Chem.* **1997**, *224*, 137–143.
(27) Berger, P. Etude du mécanisme de dissolution par oxydoréduction chimique et électrochimique des bioxydes d'actinides (UO_2, NpO_2, PuO_2, AmO_2) en milieu aqueux acide. Ph.D. Thesis, No. 1988 PA06 6073, Université Paris VI, Paris, 1988.
(28) Machuron-Mandard, X.; Madic, C. *J. Alloys Compd.* **1994**, *213*−*214*, 100–105.
(29) Joret, L.; Cote, G.; Bauer, D. *Hydrometallurgy* **1997**, *45*, 1–12.
(30) Nikitina, G. P.; Gridasov, G. C.; Listopadov, A. A.; Zhukova, I. N.; Yakovlev, V. V. *Radiochemistry* **1995**, *37*, 365–371.
(31) Lide, D. R. *Handbook of Chemistry and Physics*, 71st ed.; CRC Press: Boca Raton, FL, 1990−1991.
(32) Joseph, C.; Varghese, G.; Ittyachen, A. *J. Therm. Anal. Calorim.* **1998**, *52*, 517–522.
(33) Ollendorff, N.; Weigel, F. *Inorg. Nucl. Chem. Lett.* **1969**, *5*, 263–269.
(34) Finger, L. W. *J. Appl. Crystallogr.* **1998**, *31*, 111.
(35) Roisnel, T.; Rodriguez-Carvajal, J. *Mater. Sci. Forum* **2001**, *378*−*381*, 118–123.
(36) Barret, E. P.; Joyner, L. G.; Halenda, P. H. *J. Am. Chem. Soc.* **1951**, *73*, 373–380.
(37) Dacheux, N.; Le Du, J. F.; Brandel, V.; Genet, M.; Decambox, P.; Moulin, C. *New J. Chem.* **1996**, *20*, 507–514.
(38) Thomas, A. C.; Dacheux, N.; Le Coustumer, P.; Brandel, V.; Genet, M. *J. Nucl. Mater.* **2000**, *281*, 91–105.
(39) Lasaga, A. C. *J. Geophys. Res.* **1989**, *89*, 4009–4025.
(40) Dacheux, N.; du Fou de Kerdaniel, E.; Clavier, N.; Podor, R.; Aupiais, J.; Szenknect, S. *J. Nucl. Mater.* **2010**, *404*, 33–43.

(41) Dacheux, N.; Clavier, N.; Ritt, J. *J. Nucl. Mater.* **2006**, *349*, 291–303.
(42) Clavier, N.; du Fou de Kerdaniel, E.; Dacheux, N.; Le Coustumer, P.; Drot, R.; Ravaux, J.; Simoni, E. *J. Nucl. Mater.* **2006**, *349*, 304–316.
(43) Walther, J. V. *Am. J. Sci.* **1996**, *296*, 693–728.
(44) Ganor, J.; Mogollon, J. L.; Lasaga, A. C. *Geochim. Cosmochim. Acta* **1995**, *59*, 1037–1052.
(45) Pokrovsky, O. S.; Schott, J. *Geochim. Cosmochim. Acta* **2000**, *64*, 3313–3325.
(46) Furrer, G.; Stumm, W. *Geochim. Cosmochim. Acta* **1991**, *55*, 2193–2201.
(47) Heisbourg, G.; Hubert, S.; Dacheux, N.; Ritt, J. *J. Nucl. Mater.* **2003**, *321*, 141–151.
(48) Heisbourg, G.; Hubert, S.; Dacheux, N.; Purans, J. *J. Nucl. Mater.* **2004**, *335*, 5–13.
(49) Chou, L.; Wollast, R. *The Chemistry of Weathering*; Drever, J. I., Ed.; 1985.
(50) Chou, L.; Wollast, R. *Am. J. Sci.* **1985**, *258*, 963–993.
(51) Furrer, G.; Stumm, W. *Geochim. Cosmochim. Acta* **1986**, *50*, 1847–1860.
(52) Blum, A. E.; Lasaga, A. C. *Nature* **1988**, *331*, 431–433.
(53) Robisson, A. C.; Dacheux, N.; Aupiais, J. *J. Nucl. Mater.* **2002**, *306*, 134–146.
(54) Grenthe, I.; Puigdomenech, I. *Modelling in Aquatic Chemistry*; OECD Publications: Paris, 1997.
(55) Eyring, H. *J. Chem. Phys.* **1935**, *3*, 107–115.
(56) Rose, N. M. *Geochim. Cosmochim. Acta* **1991**, *55*, 3273–3286.
(57) Bruno, J.; Casas, I.; Puigdomènech, I. *Geochim. Cosmochim. Acta* **1990**, *55*, 647–658.
(58) De Pablo, J.; Casas, I.; Gimenez, J.; Molera, M.; Rovira, M.; Duro, L.; Bruno, J. *Geochim. Cosmochim. Acta* **1999**, *63*, 3097–3103.
(59) Hubert, S.; Heisbourg, G.; Dacheux, N.; Moisy, P. *Inorg. Chem.* **2008**, *47*, 2064–2073.
(60) Ubaldini, A.; Artini, C.; Costa, G. A.; Carnasciali, M. M.; Masini, R. *J. Therm. Anal. Calorim.* **2006**, *84*, 207–211.
(61) Higashi, K.; Sonoda, K.; Ono, H.; Sameshima, S.; Hirata, Y. *J. Mater. Res.* **1999**, *14*, 957–967.
(62) Horlait, D.; Claparède, L.; Clavier, N.; Szenknect, S.; Dacheux, N.; Ravaux, J.; Podor, R. *Inorg. Chem.* **2011**, *50*, 7150–7161.
(63) Sharov, V. A.; Bezdenezhnykh, G. V. *Usp. Khim.* **1981**, *50*, 1197.
(64) Balboul, B. A. A.; Myhoub, A. Y. Z. *J. Anal. Appl. Pyrolysis* **2010**, *89*, 95–101.
(65) Hong, S. J.; Virkar, A. V. *J. Am. Ceram. Soc.* **1995**, *78*, 433–439.
(66) JCPDS Card No. 010810792.
(67) Ikuma, Y.; Shimada, E.; Okamura, N. *J. Am. Ceram. Soc.* **2005**, *88*, 419–423.
(68) Mikulova, J.; Rossignol, S.; Gérard, F.; Mesnard, D.; Kappenstein, C.; Duprez, D. *J. Solid State Chem.* **2006**, *179*, 2511–2520.
(69) Guo, X.; Waser, R. *Prog. Mater. Sci.* **2006**, *51*, 151–210.
(70) Ostwald, W. *Z. Phys. Chem.* **1897**, *22*, 289–302.
(71) Le Coustumer, P.; Monthioux, M.; Oberlin, A. *J. Eur. Ceram. Soc.* **1993**, *11*, 95–103.
(72) Bellière, V.; Joorst, G.; Stephan, O.; de Groot, F. M. F.; Weckhuysen, B. M. *J. Phys. Chem. B* **2006**, *110*, 9984–9990.
(73) Jarcho, M.; Bolen, C. H.; Thomas, M. B.; Bobick, J.; Kay, J. F.; Doremus, R. H. *J. Mater. Sci.* **1976**, *11*, 2027–2035.
(74) Chen, J. C.; Chen, W. C.; Tien, Y. C.; Shih, C. J. *J. Alloys Compd.* **2010**, *496*, 364–369.
(75) Dollimore, D. *Thermochim. Acta* **1987**, *117*, 331–363.
(76) Wintergerst, M.; Dacheux, N.; Datcharry, F.; Herms, E.; Kapusta, B. *J. Nucl. Mater.* **2009**, *393*, 369–380.
(77) Ruas, A.; Pochon, P.; Simonin, J. P.; Moisy, P. *Dalton Trans.* **2010**, *39*, 10148–10153.
(78) Krawetz, A. Raman spectral study of equilibria in aqueous solutions of nitric acid. Ph.D. Thesis, University of Chicago, Chicago, IL, 1955.
(79) Terry, B. *Hydrometallurgy* **1983**, *11*, 315–344.
(80) Vandenborre, J.; Grambow, B.; Abdelouas, A. *Inorg. Chem.* **2010**, *49*, 8736–8748.